Mesh-free modelling of liquid crystals using modified smoothed particle hydrodynamics

YAKUTOVICH, Mikhail, CARE, Chris, NEWTON, CJP and CLEAVER, Doug <http://orcid.org/0000-0002-4278-0098>

Mesh-free modelling of liquid crystals using modified smoothed particle hydrodynamics

M.V. Yakutovich[1], C.M. Care[1], C.J.P. Newton[2] and D.J. Cleaver[1]
[1] *Materials and Engineering Research Institute, Sheffield Hallam University, Howard Street, Sheffield, S1 1WB, United Kingdom*
[2] *Hewlett-Packard Laboratories, Filton Road, Stoke Gifford, Bristol BS12 6QZ, United Kingdom*

We present a generalisation of the Modified Smooth Particle Hydrodynamics simulation technique capable of simulating static and dynamic liquid crystalline behaviour. This generalisation is then implemented in the context of the Qian-Sheng description of nematodynamics. To test the method, we first use it to simulate switching in both a Fréedericksz setup and a chiral hybrid aligned nematic cell. In both cases, the results obtained give excellent agreement with previously published results. We then apply the technique in a 3-dimensional simulation of the switching dynamics of the post aligned bistable nematic device.

PACS numbers: 61.30.-v,42.79.Kr,47.50.Cd

I. INTRODUCTION

Computer simulation has played a significant role in furthering both the fundamental understanding of liquid crystalline (LC) behaviour and the applications of ordered fluids in optical and other device applications [1]. For example, molecular simulations of hard-particle systems confirmed and quantified Onsager's prediction that shape anisotropy alone provides a sufficient condition for nematic ordering [2] and observation of biaxial nematic behaviour from generic particle simulations [3] preceded experimental claims of such a phase for small-molecule mesogens [4, 5]. At a more coarse-grained level, continuum modelling has been central to the development of devices such as the bistable ZBD cell [6, 7], and modelling has also driven exciting recent developments in the field of LC colloids [8]. There are now well-established methods for the simulation of LCs at atomistic, molecular and continuum levels [1]. Continuum level simulations are generally implemented using grid-based methods such as finite element and Lattice Boltzmann approaches, and commonly resort to reduced dimensionality. However, while these approaches can be discretised to a level that approaches the dimensions of generic molecular systems, there remain some meso-level behaviours that are not well described by any currently-available approach. For example, simulation of the dynamical behaviour of three-dimensional director field arrangements involving moving interfaces and/or LC defects remains a considerable challenge.

Mesh-free methods are a promising class of numerical techniques developed in the last decade as an alternative to traditional grid-based methods such as the finite difference method (FDM) and the finite element method (FEM). The central goal in mesh-free approaches is to find an accurate solution to appropriate partial differential equations on a set of randomly distributed points. In contrast to FEM and FDM, however, there is no need for an underlying mesh or any connections between the elements. This allows a greater range of problems to be tackled, such as free surfaces flows, moving interfaces and discontinuities, due to the relative ease of handling large deformations. Indeed, mesh-free methods appear well suited to addressing many of the multiscaling issues currently being addressed by the modelling community.

Smoothed Particle Hydrodynamics (SPH) is the oldest mesh-free method, having originally been introduced in the late 1970's to simulate unbounded three-dimensional problems in astrophysics [9, 10]. It is a truly mesh-free Lagrangian technique, which has been successfully applied to a broad range of problems such as free surface flows [11], underwater explosions [12], problems of heat conduction [13], dynamic response with material strength [14] and many other fluid and mechanical applications [15]. In spite of its wide application, it has two inherent weaknesses, namely the boundary deficiency problem and tensile instability, which have motivated the development of improved techniques. For example, the reproduced kernel particle method [16] was developed to improve the consistency of the SPH approach. Also, the Corrected Smoothed Particle Method (CSPM) [13] has addressed both the tensile instability and the inconsistency problems. More recently, Modified Smoothed Particle Hydrodynamics (MSPH) has been introduced as a further enhancement over the CSPM. This method was developed simultaneously and independently by Zhang and Batra [17] and by Liu and Liu [18], whose works should be consulted for further details.

MSPH is a promising technique which overcomes the two main problems with SPH while still retaining its best features and robustness. While MSPH is a relatively new method, it has been demonstrated to work well for the simulation of the Navier-Stokes equations for isotropic fluids [19] in a range of mechanical problems [20–22]. In this paper, we present a scheme for generalising the MSPH method to the nematodynamic simulation of LCs with variable orientational order parameter. Due to the mesh-free foundations of the MSPH approach, our generalisation can readily be implemented in 1-, 2-, or 3-dimensions. Also, due to the way the cen-

tral derivatives are calculated, addition of extra dependencies, i.e. multiphysics, is straightforward and does not introduce significant computational overhead. As implemented, the resulting algorithm includes five independent Leslie viscosities, a Landau-de Gennes free energy which introduces three or more elastic constants, a temperature dependent order parameter, surface anchoring and chirality. Adherence to, e.g., a conventional Landau-de Gennes approach is not a necessity, however, and there is scope for replacing the above with a more microscopic description capable of exhibiting thermal fluctuations.

The remainder of this paper is organised as follows. In the next two Sections, we present the Qian-Sheng description of nematodynamics and the basis of the mesh-free MSPH approach to isotropic fluid simulation. Following this, we introduce our generalised MSPH approach for ordered fluids. We then demonstrate its application by using it to simulate two quasi 1-dimensional systems. These test systems are chosen such that they allow us to compare directly with analytical solutions and, so, credibly assess the accuracy of our approach. We then report on our attempts to use this same MSPH approach to simulate the switching dynamics of the post aligned bistable nematic device (PABN). Finally, we close with some conclusions and discuss possible future extensions and applications.

II. QIAN-SHENG EQUATIONS

In this section, we outline the Qian and Sheng formulation [7, 23] for the flow of a nematic LC whose orientational order is described by a $\boldsymbol{Q}$ tensor. The Qian-Sheng formalism is a generalisation of Ericksen-Leslie–Parodi (ELP) theory complemented with Landau-de Gennes (LdG) theory, in which orientational order is described using the second rank, traceless, symmetric tensor $\boldsymbol{Q}$

$$Q_{\alpha\beta} = \frac{S}{2}\left(3\hat{n}_\alpha\hat{n}_\beta - \delta_{\alpha\beta}\right) + \frac{P_{_B}}{2}\left(\hat{l}_\alpha\hat{l}_\beta - \hat{m}_\alpha\hat{m}_\beta\right). \quad (1)$$

Here, Greek indices represent orthogonal Cartesian coordinates, while $\delta_{\alpha\beta}$ is the Kronecker delta symbol. S and $P_{_B}$ are the uniaxial and biaxial order parameters with $\hat{\boldsymbol{n}}$, $\hat{\boldsymbol{l}}$ and $\hat{\boldsymbol{m}}$ being orthogonal unit vectors associated with the principle axes of $\boldsymbol{Q}$. The director, $\hat{\boldsymbol{n}} = (\sin\theta\cos\phi, \sin\theta\sin\phi, \cos\theta)$, is the eigenvector corresponding to the largest eigenvalue of $\boldsymbol{Q}$. In the uniaxial approximation, $P_{_B} = 0$ whereas in the ELP approximation, the scalar order parameter $S \to S_0$ is a constant.

The Landau-de Gennes (LdG) free energy functional [24] is defined as

$$\begin{aligned}\mathcal{F}_{Global} &= \mathcal{F}_{Bulk} + \mathcal{F}_{Surface} = \int_\Omega \{f_B\} + \int_\Gamma \{f_S\} \\ &= \int_\Omega \{f_{LdG} + f_D + f_{EM}\} + \int_\Gamma \{f_S\}, \end{aligned} \quad (2)$$

where Ω is an open-bounded set with boundary Γ, f_B is the total bulk free energy density, f_{LdG} is the LdG free energy density of the bulk, f_D is the free energy density due to elastic contributions, f_{EM} is the term due to the effect of any applied electromagnetic field and f_S is the surface free-energy density. For simplicity, we omit any flexoelectric contributions.

The LdG bulk free energy density $f_{LdG} \equiv f_{LdG}(\boldsymbol{Q})$ is given by an expansion in the scalar invariants of the $\boldsymbol{Q}$ tensor, normally truncated at the fourth-order terms, which provides a general description effectively representing the uniaxial phase [25]:

$$\begin{aligned} f_{LdG}(\boldsymbol{Q}) &= f_{iso} + \frac{1}{2}\alpha_F Q_{\alpha\beta}Q_{\beta\alpha} - \beta_F Q_{\alpha\beta}Q_{\beta\gamma}Q_{\gamma\alpha} \\ &\quad + \gamma_F Q_{\alpha\beta}Q_{\beta\alpha}Q_{\mu\nu}Q_{\nu\mu}. \end{aligned} \quad (3)$$

Here, and in the remainder of this article, the tensor summation convention over repeated Greek indices is assumed. Here, f_{iso} is the free energy density of the isotropic fluid, and α_F, β_F and γ_F are parameters determining the phase of the thermotropic LC, which can be isotropic, nematic or biaxial.

The elastic free energy density $f_D \equiv f_D(\partial\boldsymbol{Q})$ should be invariant to arbitrary rotations or translations. This implies that not all of the combinations of $\boldsymbol{Q}$ derivatives are allowed and, thus, the distortion free energy f_D can be compactly expanded as:

$$\begin{aligned} f_D(\partial\boldsymbol{Q}) &= \frac{1}{2}L_1\partial_\mu Q_{\nu\gamma}\partial_\mu Q_{\nu\gamma} + \frac{1}{2}L_2\partial_\mu Q_{\nu\mu}\partial_\gamma Q_{\nu\gamma} \\ &\quad + \frac{1}{2}L_3\partial_\mu Q_{\nu\gamma}\partial_\gamma Q_{\nu\mu} + \frac{1}{2}L_4 Q_{\mu\nu}\partial_\mu Q_{\gamma\tau}\partial_\nu Q_{\gamma\tau} \\ &\quad + \frac{4\pi L_1}{P_{ch}}\varepsilon_{\mu\nu\gamma}Q_{\mu\tau}\partial_\nu Q_{\gamma\tau} \\ &\quad - \frac{4\pi L_4}{P_{ch}}\varepsilon_{\mu\nu\gamma}Q_{\mu\eta}Q_{\eta\tau}\partial_\nu Q_{\gamma\tau} \\ &\quad + \frac{6\pi^2}{P_{ch}^2}\left(L_1 Q_{\mu\nu}Q_{\nu\mu} - L_4 Q_{\mu\nu}Q_{\nu\tau}Q_{\tau\mu}\right), \end{aligned} \quad (4)$$

where L_i, $i = 1, \ldots, 4$ are the elastic constants and P_{ch} is the pitch of any chirality. $\varepsilon_{\alpha\beta\gamma}$ is the Levi-Civita symbol.

The free energy density in the presence of an electromagnetic field ($\boldsymbol{E}$, $\boldsymbol{H}$) is linear in the $\boldsymbol{Q}$ tensor and is written as

$$\begin{aligned} f_{EM} &\equiv f_{EM}(\boldsymbol{Q}) = -\frac{1}{3}\epsilon_0\Delta\epsilon^{max}E_\alpha Q_{\alpha\beta}E_\beta - \frac{1}{6}\epsilon_0\epsilon_{\gamma\gamma}E^2 \\ &\quad - \frac{1}{3}\mu_0\Delta\chi^{max}H_\alpha Q_{\alpha\beta}H_\beta - \frac{1}{6}\mu_0\chi_{\gamma\gamma}H^2, \end{aligned} \quad (5)$$

where $\boldsymbol{\epsilon}$ is the dielectric tensor and $\boldsymbol{\chi}$ diamagnetic tensor with $\Delta\epsilon^{max}$ and $\Delta\chi^{max}$ being the maximal anisotropies (i.e., those corresponding to $S = 1$).

The surface free energy density for weak anchoring can take several forms, the simplest being

$$f_S \equiv f_S(\boldsymbol{Q}) = \frac{W}{2}\left(Q_{\alpha\beta} - Q^o_{\alpha\beta}\right)^2, \quad (6)$$

where W is the anchoring strength and $Q^o_{\alpha\beta}$ the preferred surface order tensor. For the more complicated case of planar degenerate anchoring the following form has been suggested [26]:

$$f_S = c_1 \boldsymbol{\nu.Q.\nu} + c_2(\boldsymbol{\nu.Q.\nu})^2 + c_3 \boldsymbol{\nu.Q^2.\nu}, \qquad (7)$$

where the c_i are anchoring coefficients and $\boldsymbol{\nu}$ is the vector of the surface normal. Here, the effective anchoring strength differs slightly from the standard Rapini-Papoular form, and can be expressed as $W = \frac{2}{3}S_0(3c_1 + (c_3 - 2c_2)S_0)$.

The central equations in the Qian-Sheng formalism, which describe the evolution of momentum and order for incompressible ($\partial_\alpha u_\alpha = 0$) nematodynamics, are

$$\rho \dot{u}_\beta = \partial_\alpha \left(-P\delta_{\alpha\beta} + \sigma^v_{\alpha\beta} + \sigma^d_{\alpha\beta} + \sigma^{EM}_{\alpha\beta}\right), \qquad (8)$$

and

$$J\ddot{Q}_{\alpha\beta} = h_{\alpha\beta} + h^v_{\alpha\beta} - \lambda\delta_{\alpha\beta} - \varepsilon_{\alpha\beta\gamma}\lambda_\gamma, \qquad (9)$$

where the superposed dot ($\dot{}$) denotes the material time derivative: $\partial_t + u_\alpha\partial_\alpha$. Here, the local variables are ρ, the LC density, $\boldsymbol{u}$, the fluid velocity, P, the pressure, and J, the moment of inertia. This is usually negligible and we therefore set $J = 0$. λ and λ_γ are Lagrange multipliers chosen to ensure that $\boldsymbol{Q}$ remains symmetric and traceless. $\boldsymbol{\sigma}^d$ and $\boldsymbol{h}$ are the distortion stress tensor and molecular field defined by the LdG free energy as

$$\sigma^d_{\alpha\beta} = -\frac{\partial f_B}{\partial(\partial_\alpha Q_{\mu\nu})}\partial_\beta Q_{\mu\nu}, \qquad (10)$$

$$h_{\alpha\beta} = -\frac{\partial f_B}{\partial Q_{\alpha\beta}} + \partial_\gamma \frac{\partial f_B}{\partial(\partial_\gamma Q_{\alpha\beta})}. \qquad (11)$$

$\boldsymbol{\sigma}^v$ and $\boldsymbol{h}^v$, the viscous stress tensor and viscous molecular field, are given by

$$\begin{aligned}\sigma^v_{\alpha\beta} &= \beta_1 Q_{\alpha\beta}Q_{\mu\nu}A_{\mu\nu} + \beta_4 A_{\alpha\beta} + \beta_5 Q_{\alpha\mu}A_{\mu\beta} \\ &+\beta_6 Q_{\beta\mu}A_{\mu\alpha} + \frac{\mu_2 N_{\alpha\beta}}{2} - \mu_1 Q_{\alpha\mu}N_{\mu\beta} \\ &+ \mu_1 Q_{\beta\mu}N_{\mu\alpha}, \end{aligned} \qquad (12)$$

and

$$h^v_{\alpha\beta} = -\frac{1}{2}\mu_2 A_{\alpha\beta} - \mu_1 N_{\alpha\beta}. \qquad (13)$$

Here β_i, μ_i are viscosities coefficients which can be directly mapped on to ELP viscosities using the dependencies given in [23], while $N_{\alpha\beta} = \dot{Q}_{\alpha\beta} - \varepsilon_{\alpha\mu\nu}\omega_\mu Q_{\nu\beta} - \varepsilon_{\beta\mu\nu}\omega_\mu Q_{\alpha\nu}$. $A_{\alpha\beta} = \frac{1}{2}(\partial_\alpha u_\beta + \partial_\beta u_\alpha)$ and $W_{\alpha\beta} = \frac{1}{2}(\partial_\alpha u_\beta - \partial_\beta u_\alpha)$ are the symmetric and anti-symmetric velocity gradient tensors with the vorticity being $\omega_\gamma = \frac{1}{2}\varepsilon_{\gamma\alpha\beta}W_{\alpha\beta}$.

$\boldsymbol{\sigma}^{EM}$ is the stress tensor arising from externally applied electromagnetic fields

$$\begin{aligned}\sigma^{EM}_{\alpha\beta} &= \frac{1}{2}(H_\alpha B_\beta + H_\beta B_\alpha) - \frac{H_\gamma B_\gamma}{2}\delta_{\alpha\beta} \\ &+\frac{1}{2}(E_\alpha D_\beta + E_\beta D_\alpha) - \frac{E_\gamma D_\gamma}{2}\delta_{\alpha\beta}, \end{aligned} \qquad (14)$$

where $\boldsymbol{E}$ ($\boldsymbol{H}$) is the electric (magnetic) field strength, $\boldsymbol{D}$ the electric displacement vector and $\boldsymbol{B}$ the magnetic flux density.

Direct calculation of the trace and off-diagonal elements of Eq. (9) shows that the Lagrange multipliers are given by $\lambda = \frac{1}{3}(h_{\gamma\gamma})$ and $\lambda_\gamma = \frac{1}{2}\varepsilon_{\alpha\beta\gamma}h_{\alpha\beta}$.

Following [27], the viscous stress tensor and the equation of motion Eq. (9) can be recast in the alternative form

$$\begin{aligned}\sigma^v_{\alpha\beta} &= \beta_1 Q_{\alpha\beta}Q_{\mu\nu}A_{\mu\nu} + \beta_4 A_{\alpha\beta} + \beta_5 Q_{\alpha\mu}A_{\mu\beta} \\ &+\beta_6 Q_{\beta\mu}A_{\mu\alpha} + \frac{\mu_2 h_{\alpha\beta}}{2\mu_1} - \frac{\mu_2\lambda\delta_{\alpha\beta}}{2\mu_1} - \frac{\mu_2\varepsilon_{\alpha\beta\gamma}\lambda_\gamma}{2\mu_1} \\ &-\frac{\mu_2^2 A_{\alpha\beta}}{4\mu_1} - Q_{\alpha\mu}h_{\mu\beta} + Q_{\alpha\mu}\varepsilon_{\mu\beta\gamma}\lambda_\gamma + \frac{\mu_2 Q_{\alpha\mu}A_{\mu\beta}}{2} \\ &+Q_{\beta\mu}h_{\mu\alpha} - Q_{\beta\mu}\varepsilon_{\mu\alpha\gamma}\lambda_\gamma - \frac{\mu_2 Q_{\beta\mu}A_{\mu\alpha}}{2}, \end{aligned} \qquad (15)$$

$$\begin{aligned}\dot{Q}_{\alpha\beta} &= \frac{h_{\alpha\beta}}{\mu_1} - \frac{\lambda\delta_{\alpha\beta}}{\mu_1} - \frac{\varepsilon_{\alpha\beta\gamma}\lambda_\gamma}{\mu_1} - \frac{\mu_2 A_{\alpha\beta}}{2\mu_1} \\ &+\varepsilon_{\alpha\epsilon\lambda}\omega_\epsilon Q_{\lambda\beta} + \varepsilon_{\beta\epsilon\lambda}\omega_\epsilon Q_{\alpha\lambda} \end{aligned} \qquad (16)$$

which is better suited to mesh-free simulation,

Finally, we state the equations imposed on the boundaries. As a rule, we impose non-slip boundary conditions on the velocity. For infinitely strong anchoring, the $\boldsymbol{Q}$ tensor is specified according to Eq. (1), in which the required director and order parameter value S are kept fixed. In cases of weak anchoring, however, the order tensor at the surface evolves according to

$$\mu_S \partial_t Q_{\alpha\beta} = h^S_{\alpha\beta} - \lambda^S\delta_{\alpha\beta} - \varepsilon_{\alpha\beta\gamma}\lambda^S_\gamma \qquad (17)$$

where $h^S_{\alpha\beta} = -\frac{\partial f_B}{\partial(\partial_\tau Q_{\alpha\beta})}\hat{\nu}_\tau - \frac{\partial f_S}{\partial Q_{\alpha\beta}}$, $\lambda^S = \frac{1}{3}h^S_{\gamma\gamma}$, $\lambda^S_\gamma = \frac{1}{3}\varepsilon_{\alpha\beta\gamma}h^S_{\alpha\beta}$, $\hat{\boldsymbol{\nu}}$ is an outward pointing surface unit normal vector and μ_S is the surface viscosity defined through $\mu_S = \mu_1 l_S$, where l_S is a characteristic surface length typically in the range $l_S \approx 100 - 1000$ [28]. We note that it has been shown that such use of localised boundary terms as a means of imposing weak anchoring can lead to numerical instabilities when discontinuous changes are made to applied bulk field terms [29]. Nevertheless, we have persisted with this approach since, as observed by Fang and co-workers [30], such anomalies are inherent in the formulation of a coherent continuum approach. Further, for the parameters and setups considered here, we have seen no significant or long-lived surface-region anomalies in our simulations when bulk field terms have been switched. As a result, there does not appear to be a strong case here for adopting a distributed approach to imposing surface viscosity.

III. THE MSPH METHOD

Before describing its implementation in the context of the Qian-Sheng equations of nematodynamics, we first

rehearse the fundamentals of the MSPH approach [17, 18]. We assume the following conventions: f_i denotes the value of a function f at point (or particle) i, $f_{,\alpha}$ denotes a derivative of the function f with respect to α and x^α denotes the α-coordinate of a vector $\boldsymbol{x}$. The main concept underlying SPH techniques is the assumption that any sufficiently smooth field variable f can be interpolated over a spatial domain Ω using a weight-function-based integral representation. This allows the action of the differentiation operator to pass from the function itself to the weight function. Further, the resultant interpolated function can be discretised onto a set of randomly distributed points to give a stable and robust model which can be implemented using dynamic particle-based simulation methods.

To show this in more detail, we consider a general Taylor expansion of an arbitrary, smooth function f near a fixed point $\boldsymbol{x}_i$ in d-dimensional space. From this, we obtain, for $f_i = f(\boldsymbol{x}_i)$:

$$f(\boldsymbol{x}) \simeq f_i + f_{i,\alpha}(x^\alpha - x_i^\alpha) + \ldots, \tag{18}$$

where α ranges from 1 to d and $f_{i,\alpha} = \partial f/\partial x_i^\alpha$. Multiplying both sides of Eq. (18) with a smoothing function (or weight function) $W = W(\boldsymbol{x}_i - \boldsymbol{x}, h)$ or its first-order derivative $W_{,\gamma} = \partial W/\partial x^\gamma$, and then integrating over the problem space Ω yields

$$\begin{aligned}
\int\limits_\Omega f(\boldsymbol{x}) W \mathrm{d}V &\simeq f_i \int\limits_\Omega W \mathrm{d}V + f_{i,\alpha} \int\limits_\Omega (x^\alpha - x_i^\alpha) W \mathrm{d}V, \\
\int\limits_\Omega f(\boldsymbol{x}) W_{,\gamma} \mathrm{d}V &\simeq f_i \int\limits_\Omega W_{,\gamma} \mathrm{d}V + f_{i,\alpha} \int\limits_\Omega (x^\alpha - x_i^\alpha) W_{,\gamma} \mathrm{d}V.
\end{aligned} \tag{19}$$

These integrals can be calculated at an arbitrary set of points i using the standard SPH discretisation process

$$\int\limits_\Omega f(\boldsymbol{x}) W \,\mathrm{d}V \to \sum_j f_j W_{ij} m_j/\rho_j, \tag{20}$$

where $W_{ij} = W(\boldsymbol{x}_i - \boldsymbol{x}_j, h)$, and the summation runs over the neighbours in the support domain of each specified point i. Typically, the smoothing function W has a compact support domain, defined by the smoothing length h.

In the conventional SPH method, Eq. (20) is used as the main method of approximation. This leads to a dynamic particle-based simulation model (a particle being associated with each point i) which is well suited to unbounded systems. Modifications need to be introduced, however, to remedy deficiencies associated with, e.g., boundary conditions and tensile instability. In the main, such modifications have been introduced at the particle-model level. There is no established route to implementing these, however, and some of these modifications have been criticised as being arbitrary and shown to worsen some problems while solving others.

In contrast, the more holistic MSPH approach avoids such difficulties by retaining all of the terms in eqns (19). This both improves the accuracy of the method and gives a rigorous approach for the implementation of boundaries. This improvement comes, though, at the cost of some extra computational effort, since the values of the function f and its derivatives now need to be evaluated at each point from the set of linear equations

$$\mathbf{BF} = \mathbf{T}. \tag{21}$$

For the three-dimensional case, the matrices $\mathbf{B}$, $\mathbf{F}$ and $\mathbf{T}$ are

$$\begin{aligned}
&B_{IJ} = \sum_{j=1}^{N} \Phi(I)\Theta(J)\frac{m_j}{\rho_j}, \;\; T_I = \sum_{j=1}^{N} f_j \Phi(I) \tfrac{m_j}{\rho_j}, \\
&F = \{f_i, f_{i,x}, f_{i,y}, f_{i,z}\}^T, \qquad I, J = 1, 2, 3, 4
\end{aligned} \tag{22}$$

$$\begin{aligned}
\Phi(1) = W_{ij}, \quad \Phi(2) = W_{ij,x}, \\
\Phi(3) = W_{ij,z}, \quad \Phi(4) = W_{ij,y} \\
\Theta(1) = 1, \;\; \Theta(2) = x_j - x_i, \\
\Theta(3) = y_j - y_i, \;\; \Theta(4) = z_j - z_i.
\end{aligned} \tag{23}$$

The system of simultaneous linear equations (21) has a solution at each interpolation point provided that the matrix $\mathbf{B}$ is not ill-conditioned. The method's accuracy can be further improved by retaining higher-order derivatives in the Taylor expansion eqn. (18). This, though, again introduces additional computational effort, since the number of linear equations in (21) increases accordingly.

Partial differential equations describing real physical phenomena very often include higher order derivatives. For example, eqn. (8) in the Qian-Sheng description effectively contains third order derivatives. In the MSPH approach, these can be calculated in two different ways. Firstly, the derivatives can be calculated directly by retaining all terms up to the required order in the Taylor expansion of the field function (18). This approach is computationally expensive, since the number of equations in (21) increases rapidly with both the number of expansion terms and the problem's dimensionality. An alternative approach is to calculate higher order derivatives directly as first-order derivatives of the lower order derivatives. This nested approximation retains the same order of accuracy as the full solution and is, therefore, our preferred approach in the calculations presented here.

As indicated in Section I, a number of alternative mesh-free methods have been developed since the original appearance of the SPH model. An interesting and useful feature of the MSPH and SPH solvers which is not found in other mesh-less techniques is that weight functions of the former are always positive. In mesh-free methods which do not have this feature, constructions based on weight functions can lead to negative values of density, energy, etc. in certain regions. While this is mathematically sound, it leads to non-physical behaviours which, when particle-based simulation methods are used, can effectively break the physical simulation.

Conversely, fluid particles, or interpolation points, in the MSPH approach can always be taken to have real masses and to move in a problem space according to forces and torques calculated from pair-wise particle-particle interactions. In our implementation, these follow naturally from eqn. (8). These fluid particles have a real volume ΔV but do not have fixed shape. As well as having unambiguous physical meaning, this additionally opens up possibilities for multiscaling.

In the simulation of flows using the SPH approach, spurious oscillations can occur in both the velocity and pressure fields. These numerical instabilities originate from algorithmic pathologies in the approximations used for parabolic or hyperbolic systems. Sometimes, these can be resolved by the introduction of an artificial viscosity. When, in preliminary work, we applied the basic SPH approach to simulate the Qian-Sheng equations, we observed significant numerical instabilities even after the introduction of an artificial viscosity. These proved to derive from the rather complex nature of the driving equations. Also, the low accuracy of the SPH method near to or at system boundaries made it impossible to impose anything more complex than Dirichlet boundary conditions. This line of work was therefore abandoned, on the basis that it was not capable of yielding an LC simulator fit for purpose, and the more complex MSPH approach adopted instead.

From a mathematical point of view, MSPH is simply a tool for solving partial differential equations at a set of randomly distributed points. The method's accuracy usually increases with increase in the number of interpolation points in a given region. Combination of these two aspects leads to an interesting property of the MSPH method: the method's resolution automatically increases in regions where flow is directed. We believe this can be an important feature for an MSPH model of LCs, especially for the modelling of defects.

By its nature, MSPH is an adaptive and Lagrangian mesh-free method in which particles are free to move. In some problems, however, the particles can be held fixed in space. This feature is relevant to the simulation of LCs in situations where Q evolution (governed via eqn (16)) needs to be considered but the velocity field (governed via eqn (8)) can be neglected. In such a circumstance, the computational effort involved is greatly decreased, since the matrix $\mathbf{B}$ in Eq.(21) needs to be estimated only once. The method's accuracy can be further improved by appropriate tuning of the smoothing length h and achieving a uniform distribution of the particle positions [18]. It has been shown that, in such circumstances, the method's accuracy can exceed that of FEM approaches [21]. In other cases, however, such as free surface flows, and systems involving high gradients, multi-resolution, complex geometries etc. the full Lagrangian description with free moving particles is needed.

IV. MSPH NEMATODYNAMICS

We now describe the algorithm we have developed to simulate LC behaviour using the MSPH technique. The core algorithm is explained in Sec. IV A. The way we solve electric field is then described in Sec. IV B while the implementation of boundary conditions is described in Sec. IV C.

A. The algorithm description

In order to solve the Qian-Sheng equations of Sec. II we additionally associate a traceless, symmetric, order tensor, $Q_{\alpha\beta}$, with each fluid particle. Microscopically, these order tensors convey information about the state of the average orientational ordering of the molecules which are assumed to be represented by each fluid particle.

The resulting simulation algorithm centres, then, on solving the set of Qian-Sheng eqns. (8)-(17) on a set of randomly distributed points in 1-, 2-, or 3-dimensions using the MSPH method described in Sec. III. Initially, particles are uniformly located on a problem's domain and are given starting values of velocity, density and Q. Then, eqns. (8) and (16) are considered for each particle, with their right-hand sides replaced by the appropriate kernel estimates. We use the nested approach to calculate the derivatives involved in these, and retain all of the derivatives in the Taylor expansion (18) up to the second order. We have found that retaining third order derivatives does not significantly improve the model's accuracy, whereas it does add an appreciable computational overhead.

Firstly, we estimate the velocity gradients, and thus find $A_{\alpha,\beta}$, $N_{\alpha,\beta}$. After that, knowing all Q derivatives up to second order, we estimate all stress tensors on the right hand side of Eq. (8) and the molecular field $h_{\alpha\beta}$ on the right hand side of Eq. (16). Finally, we calculate the right-hand side of Eq. (8) by estimating the first order derivatives. We adopt a simple two step predictor-corrector scheme to integrate the resulting linear ordinary differential equations to second order accuracy.

As noted above, in some LC problems there is no need to calculate the velocity field, i.e. if one is interested only in solving the flow-free Q-field described by Eq. (16). In such cases, we can set all initial velocities to zero and keep the simulated particles fixed in space. This approach significantly reduces the computational effort required since it avoids the extra loop associated with the estimation of the derivatives in Eq. (8). In circumstances such as this, MSPH is employed as a purely mathematical technique which calculates derivatives on a set of randomly distributed points, and the positivity of the weight function is not exploited.

SPH was originally introduced for problems with small dissipation. In the standard SPH formulation, an artificial viscosity is usually introduced when simulating liquids. This artificial viscosity is added to the pressure

term in order to resolve shocks numerically and so prevent nonphysical particle penetrations in the event of any high velocity, head-on collisions. In the MSPH formulation, however, there is no need to use an artificial viscosity since proper viscosity terms appear in Eq. (8). It is also pertinent that there are no large velocities in typical LC simulations.

In practice, the choice of particle separation has a direct influences on both the accuracy of the final solution and the computational efficiency. For this reason, we have developed a criterion for determining how particle separation should be set in runs employing fixed particle locations. This issue is especially pertinent to the simulation of complex LC structures since in these it is generally the case that the relevant characteristic lengths can vary across the system. For example, large order tensor gradients found in the vicinity of orientational defects require a high density of points (the characteristic length is short) whereas the order in the mid-region of a twisted nematic cell can be well-described with a low point density (the characteristic length is large). Whilst it is possible to derive an analytical expression to gauge MSPH particle density for some simple systems, this is a highly non-trivial task for an LC model based on the Qian-Sheng equations. In our simulations, therefore, we have used the condition number of matrix B from eq. (21) as a key parameter by which to set the local density density of particles. Specifically, we have imposed the requirement that these condition numbers lie in the range 25 to 100. We have found that systems become prone to numerical instabilities when the condition numbers exceed 100, but that this is remedied by increasing the particle density. Conversely, whilst condition numbers below 25 lead to some improvements in accuracy, these do not justify the associated computational cost, so we normally decrease the local particle density as a compromise between accuracy and efficiency.

In the MSPH approach, it is necessary to use the quasi-incompressible equation of state for incompressible fluids, since fluid pressure is an explicit function of local fluid density and use of the actual equation of state necessitates adoption of a very small time step. While LCs are incompressible, in our simulations they are treated as slightly compressible via the artificial equation of state. For this, we use the equation of state due to Morris et. al. [31]

$$P = c^2 \rho, \tag{24}$$

where c is the speed of sound.

We use the B-spline weight function due to Monaghan and Lattanzio [32] in our simulations

$$W(R,h) = \alpha_d \times \begin{cases} \frac{2}{3} - R^2 + \frac{1}{2}R^3 & 0 \le R < 1 \\ \frac{1}{6}(2-R)^3 & 1 \le R < 2 \\ 0 & R \ge 2 \end{cases} \tag{25}$$

where α_d is a normalisation factor which is equal to $1/h$, $15/(7\pi h^2)$ and $3/(2\pi h^3)$ in 1-, 2- and 2-dimensions, respectively. To date, this has been the most widely used kernel function in the SPH literature and it has been shown to give good results in the MSPH simulations of Ref. [21]. We employ a smoothing length h which is 1.1 times larger than the initial particle separation. When particles i and j have different smoothing lengths h_i and h_j, their interaction is symmetrised by using a mean smoothing length $h_{ij} = (h_i + h_j)/2$.

B. Electric field implementation

LCs are anisotropic dielectric and diamagnetic media and their dielectric permittivities and magnetic susceptibilities are different along the directions parallel and perpendicular to the LC director. Thus, when an external voltage is applied to a model LC device, it is necessary to solve Maxwell's equations in order to determine the electric field $\boldsymbol{E}$ at each interpolation point. The equations we solve are

$$\begin{aligned} \partial_\alpha D_\alpha &= 0, \\ D_\alpha &= \epsilon_0 \epsilon_{\alpha\beta} E_\beta, \\ E_\beta &= -\partial_\beta V, \\ \epsilon_{\alpha\beta} &= (2\Delta\epsilon^{max} Q_{\alpha\beta} + \epsilon_{\gamma\gamma}\delta_{\alpha\beta})/3, \end{aligned} \tag{26}$$

where V is the local potential and $\epsilon_{\gamma\gamma} = 2\epsilon_\perp + \epsilon_\parallel$. In general, these equations need to be solved at a randomly distributed set of points. In order to achieve this, we first employ MSPH to calculate all of the derivatives appearing in Eqs. (26). We then solve Eqs. (26) numerically using a successive over-relaxation method at each time-step when the Q-tensors are known at each particle. Usually, only a few iterations are needed at each time-step in order to achieve the required accuracy. An external electric field is applied by imposing boundary conditions of the form $V = \text{const}$.

C. Boundary conditions

Boundary condition implementation is always a non-trivial task in mesh-free methods and there is no universal approach for imposing same. Unlike mesh-based methods, boundaries in mesh-free methods are not discretised, but rather are represented by particles. Since most mesh-free techniques have non-local interpolations as their foundation, the consequent lack of particles near to boundaries usually leads to accuracy deterioration in adjacent regions. This is especially pronounced in the original SPH method, which does not even achieve zeroeth-order consistency at boundaries. This situation is greatly improved in the MSPH method, where the consistency condition at and near to a boundary depends on both the number of higher order derivatives retained in Eq. (18) and the placement of the boundary particles.

We use virtual or ghost particles [15] to implement boundary conditions. Unlike the interior particles, these boundary particles are always held fixed in space. They

then contribute in the normal way to the interactions of the interior particles as well as exerting a penalty force similar to the Lennard-Jones interatomic potential [14], to prevent the interior particles from penetrating the boundary.

In the case of infinitely strong orientational anchoring, the Q-tensor held is fixed at boundary particles $Q_{\alpha\beta}$ = const. This amounts to imposition of simple Dirichlet boundary conditions. In the case of weak anchoring, however, the Q-tensor at the boundary particles is left free to evolve in accordance with Eq. (17). Since Eq. (17) is based on first order derivatives, the accuracy of its solution at the boundary is the same as that achieved in the bulk when using the MSPH. This consistency makes the implementation of weak anchoring boundary conditions reasonably straightforward.

V. NUMERICAL EXAMPLES

In this section we present two initial examples to demonstrate the application of the algorithms just described and assess their validity for the modelling of electro-optical devices. Due to the relatively complex nature of the partial differential equations describing LC phenomena, we limit ourselves here to quasi 1-dimensional examples which can be partly compared either with analytical solutions or with previous simulations. Our ultimate goal is to apply our MSPH nematodynamics approach to a range of physical and device phenomena; its use to simulate 3-dimensional applications and these will be addressed in future publications is therefore examined in Sec. VI.

In Sec. V A we demonstrate application of the method to the simulation of the classic Fréedericksz transition in order to assess both electric field and Q-solvers while neglecting flow. In Sec. V B we then simulate the behaviour of a dual-frequency chiral hybrid aligned nematic LC cell, in order to validate the full implementation of the MSPH solver (i.e. with flow included).

A. Fréedericksz Transition

We first consider the splay geometry variant of the well known Fréedericksz transition behaviour. In this, we switch off the velocity field and consider only the evolution of the Q-tensor and electric field as the applied voltage is varied. In order to maintain consistency with analytical treatments, we assume infinite anchoring boundary conditions on both plates, with the director fixed parallel to the plates.

In the splay geometry, the critical Fréedericksz voltage V_c is given by

$$V_c = \pi\sqrt{\frac{K_{11}}{\epsilon_0\Delta\epsilon}}, \tag{27}$$

where $\Delta\epsilon$ is the LC's dielectric anisotropy and K_{11} is the splay elastic constant.

For an applied voltage $\overline{V} > V_c$ the maximum distortion angle θ_m of the director in the centre of the cell can be found numerically from the following equation [33, 34]

$$\frac{V}{V_c} = \frac{2(1+\gamma\sin^2\theta_m)^{\frac{1}{2}}}{\pi}\int_0^{\frac{\pi}{2}} \frac{G(\theta_m,\kappa,\gamma,\lambda)}{(1+\gamma\sin^2\theta_m\sin^2\lambda)^2}\,d\lambda, \tag{28}$$

where $\gamma = \Delta\epsilon/\epsilon_\perp$, $\kappa = (K_{33}-K_{11})/K_{11}$ and

$$G(\theta_m,\kappa,\gamma,\lambda) = \frac{(1+\kappa\sin^2\theta_m\sin^2\lambda)(1+\gamma\sin^2\theta_m\sin^2\lambda)}{1-\sin^2\theta_m\sin^2\lambda}. \tag{29}$$

The resulting equilibrium director profile can then be determined from

$$\overline{z} = \frac{1}{2}\frac{\int_0^{\phi} G(\theta_m,\kappa,\gamma,\lambda)^2\,d\lambda}{\int_0^{\frac{\pi}{2}} G(\theta_m,\kappa,\gamma,\lambda)^2\,d\lambda},\ \phi = \sin^{-1}\left(\frac{\sin\theta}{\sin\theta_m}\right), \tag{30}$$

where $\overline{z} = z/d$ is the reduced distance. In the above equation, $0 \le \overline{z} \le \frac{1}{2}$; the solution for $\frac{1}{2} \le \overline{z} \le 1$ is obtained from the symmetry condition $\theta(\overline{z}) = \theta(1-\overline{z})$. Equations (28,30) were derived using an assumption of fixed order parameter. Despite this, we use them here to compare with our results since, in our simulations of this system, the maximal change in order parameter we have observed is 0.002.

Inserting the uniaxial order tensor definition into eqn (3) and making the usual assumptions of linear temperature dependance of the first Landau-de Gennes coefficient, leads to the algorithmically convenient form

$$f_{LdG}(\boldsymbol{Q}) = f_{iso} + a(T-T^*)S^2 - BS^3 + CS^4 \tag{31}$$

where $a(T-T^*) = 3\alpha_F/4$, $B = 3\beta_F/4$, $C = 9\gamma_F/4$ and $T^* = T_{NI} - B^2/4aC$. Setting these coefficients to a = 65000 J m^{-3} K^{-1}, B = 530000 J m^{-3}, and C = 980000 J m^{-3}, which are suitable for 5CB [35], with elastic constant values (K_{11} = 17, K_{22} = 13, K_{33} = 30) $\times 10^{-12}$ N, we have simulated the Fréedericksz effect for a cell of width $d = 1$ μm at temperature $T = T_{IN} - 4(T_{IN} - T^\star)$. In order to achieve a marked response to the applied field, we have set the dielectric anisotropy to be relatively large $\Delta\epsilon = 10.3$, with $\epsilon_\parallel = 12.87$ and $\epsilon_\perp = 2.57$. For this choice of parameters, the critical Fréedericksz voltage is 1.36 V.

The evolution of the director profile for a uniformly-spaced 100 point simulation of this system on application of a 3 V potential to an initially uniform LC cell is shown in Fig. (1). These profiles represent snapshots taken from a run performed with a time-step of 10^{-7} s. The corresponding equilibrium director profile determined from eqn. (30) is also shown, and is in excellent agreement with the long-time simulation profile. The Q-solver element of this simulation was computationally very efficient, and the bulk of the run-time was taken up by the relatively rudimentary E-field solver used here.

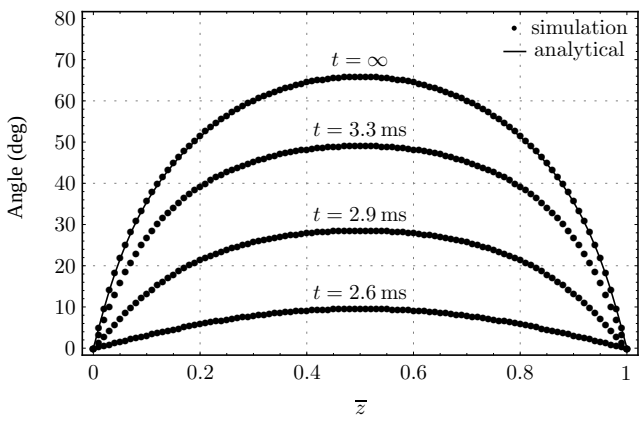

FIG. 1: Time evolution of the angle which director makes with x-axis across the cell. Analytical curve in equilibrium is found from Eq. (30).

TABLE I: Table of the percentage error in the simulated director angle in the cell centre depending on the number of interpolation points and their distribution (uniform and non-uniform). An analytical value of 65.66° is found from eqn. (28).

Number of points	Uniform distribution, percentage error	Non-uniform distribution, percentage error
30	3.4	1.1
50	1.4	0.7
70	0.8	0.5
100	0.5	0.3

In order to assess the effect of the number and distribution of the interpolation points on the accuracy of this simulation, we have performed a number of equivalent runs and found that small discrepancies can arise when regions with high director gradients have low point density. We quantify this effect in Table I which shows the percentage overshoot in the central director angle obtained for different choices of point distribution. This error is reduced below 0.5% for 100 uniformly spaced points or 70 non-uniformly spaced points. Here, a simple arithmetic progression was used to concentrate the non-uniform point distribution on the region with high director gradient, but it would be straightforward to implement a scheme which iteratively distributed points according to their local Q gradients.

Finally, in this Section, we note that time-dependant profiles of the electric potential are routinely determined in our method. We illustrate this behaviour in Fig. (2). Initially, when Q is uniform across the cell, the electric field is necessarily constant, leading to a linear potential profile. As $Q(\overline{z})$ develops splay-bend distortions, however, the field becomes concentrated in those regions with highest dielectric constant, leading to marked nonlinearities in the electric potential $V(\overline{z})$. There is no analytical formula for the time-dependent electric potential across the Fréedericksz cell.

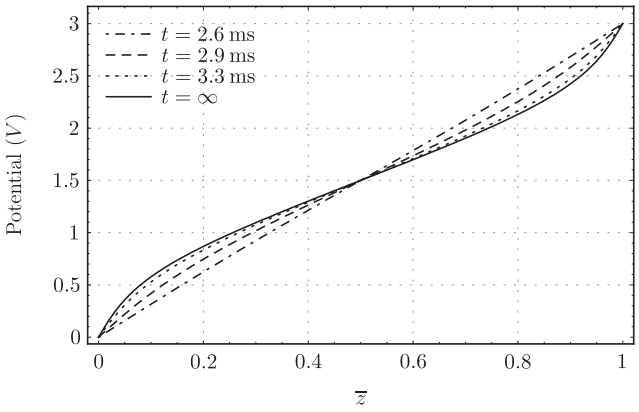

FIG. 2: Time evolution of the electric potential across the Fréedericksz cell.

B. Fast switching dual-frequency chiral HAN cell

Having validated the order-tensor aspects of our MSPH approach against the standard Fréedericksz setup, we now assess the full model by turning on the flow effects. To illustrate this, we consider the switching of a dual-frequency chiral hybrid aligned nematic liquid-crystal cell (CHAN) [36, 37]. In such a device, a chiral LC with a frequency-dependant dielectric permittivity is used, so as to achieve fast switching times. The principles underlying the operation of this device are that both of its switching behaviours are field driven, whereas the relaxation of a simple Fréedercksz cell is a passive process whose speed is dictated by material properties such as elastic constants and viscosity coefficients. The two states of the CHAN device are zero field chiral HAN arrangement and a high-frequency-field-induced twisted nematic arrangement. Both states are accessed from the same intermediate vertically aligned state, induced by a low frequency field pulse.

This CHAN system was chosen as a test for our full MSPH LC simulator because, as we demonstrate below, its behaviour is strongly dependant on the velocity field. It therefore gives us the opportunity to assess the ability of the MSPH approach to properly recover the physical nature of the partial differential equations describing LC flow (i.e. eqn. (8)). Note that the partial differential equations governing the LC description used for this system also necessarily contain terms introducing chirality. A further reason for considering the CHAN set-up is that it has recently been the subject of a combined experimental and theoretical study by Sambles and Jewell [36, 37]. Here, therefore, we are able to adopt the same cell and material parameters as were used in refs [36, 37] and make a direct comparison with their results. Thus, the cell width is set at 4.94 μm, with homeotropic anchoring on one surface and planar anchoring on the other. The elastic constants used are $(K_{11} = 16.7,\ K_{22} = 10,\ K_{33} = 20.9) \times 10^{-12}$ N and the pitch is $P_{ch} = 13.0$ μm. The viscosity coefficients

are ($\alpha_1 = -10$, $\alpha_2 = -300$, $\alpha_3 = 25$, $\alpha_4 = 170$, $\alpha_5 = 190$, $\alpha_6 = -85$) $\times 10^{-3}$ kg m^{-1} s^{-1} and the density is $\rho = 1.01 \times 10^3$ kg m^{-3}. The dielectric anisotropies are $\Delta\epsilon = 2.6$ at low frequency and $\Delta\epsilon = -2.3$ at high frequency. The modelling work presented in refs [36, 37] was based on the Leslie-Eriksen-Parodi director-based description of nematodynamics, and achieved by iteratively time-stepping through the velocity and orientation profile variations.

Initially, we have obtained the CHAN cell's equilibrium configuration by setting the LC alignment to be uniform except at the boundaries, which were fixed at homeotropic and planar, and letting the Q tensor evolve in the absence of an applied field. In the course of time, the order tensor arrangement then relaxed to the equilibrium configuration. To allow meaningful comparison of our data with those of [36], we have used our particle Q tensors to construct director tilt and azimuthal angle profiles; for the equilibrium configuration, these are plotted in Figs. 3 (a,b) with the time label $t = 0$. Slight non-linearities are apparent here, reflecting the difference in the splay and bend elastic constants.

Following [36], we then applied a low-frequency 7 V pulse to the system for 20 ms immediately followed by a high frequency pulse with the same voltage for 80 ms. The twist and tilt profiles obtained during these two time windows are shown in Figs. 3. Like ref [36], we have held all z-components of the velocity at zero in our 1-dimensional modelling of this device. In contrast to [36], however, we have embedded dielectric permittivities within our model and simply imposed constant applied voltages. Due to both this and the Q-tensor nature of our model, while we expect the qualitative behaviour observed here to be equivalent to that seen by Sambles and Jewell, small quantitative discrepancies can be anticipated.

When the low-frequency voltage was applied to this CHAN system, the director tilt profile (Fig. 3a) switched monotonically from approximately linear to tanh-like, the action of the applied field being to promote homeotropic alignment in the upper half of the cell. The accompanying changes in the associated twist profiles (Fig. 3b) have little physical significance since they predominate in the growing homeotropic region in which twist is relatively meaningless. When we ran an equivalent simulation with all velocities set to zero, no differences were apparent in the initial and final low-frequency-field profiles, but the intermediate profiles showed slower convergence in the homeotropic region.

When the frequency of the applied voltage was changed, at $t = 20$ ms, a backflow effect was produced which significantly influenced the director profiles. This is particularly apparent from Fig. 3 (d) which shows a large jump in the twist profile immediately after the frequency shift. Physically, this corresponds to the director tilting backwards, leading to an instantaneous 180 degree step in the twist values observed at high z. This led to a region with high twist gradient forming in the central region of the cell, which itself promoted formation of a maximum in the associated tilt profile. Subsequently, these high twist gradient and high tilt features dilated and the cell relaxed into what was, predominantly, a twisted nematic arrangement. To illustrate the backflow behaviour responsible for these director profile rearrangements, we plot, in Fig. 4, a series of profiles of the x-component of the velocity during application of the high frequency applied field. By comparing these with Fig. 3 (c), it can be seen that the peaks in the director tilt profiles correspond to the maxima in this velocity field. Furthermore, by conducting equivalent simulations with the velocity field switched off, we have found that no twist jumps or tilt maxima are observed when backflow is suppressed. This is entirely consistent with the findings of Sambles and Jewell.

VI. PABN SWITCHING BEHAVIOUR

In this section we apply our MSPH technique to the switching dynamics of the PABN device. The PABN device is a LC cell in which one substrate is flat whereas the other is populated with an array of microscopic posts, as depicted in the micrograph Fig. 5. This cell arrangement leads to bistability, i.e. there are two optically distinct long-lasting field-off states [38], which are further referred to as planar ($\mathcal{P}$) and tilted ($\mathcal{T}$).

Experimentally, switching between these bistable states is achieved via the application of monopolar square electric field pulses, the sign of which dictates the final state. Bidirectional switching is only possible with negative dielectric LC materials. A positive pulse is needed in order to achieve $\mathcal{T}$ – $\mathcal{P}$ switching, while a negative pulse is needed to switch from $\mathcal{P}$ to $\mathcal{T}$ state. The flat substrate imposes homeotropic boundary conditions, i.e. it fixes the director to be strictly perpendicular to the surface plane. The boundary conditions on the lower substrate are of a tangent type, which restricts the director locally to be in the plane of the surface.

We have previously reported MSPH simulations of static configurations of the PABN device [40]. Here we extend these by investigating the PABN $\mathcal{T}$ – $\mathcal{P}$ switching behaviour. In this, we use an identical geometry setup to that described in [40]. Periodic boundary conditions are imposed in the x and y directions, the xy repeat unit representing a single post. We describe the height h of the post as a function of the x and y coordinates using the functional form:

$$\begin{aligned} h(x,y) \;=\; & \tanh\left(\pi\left(s_1 x - p_1\right) - \tanh\left(\pi\left(s_2 x + p_2\right)\right)\right) \times \\ & \tanh\left(\pi\left(s_1 y - p_1\right) - \tanh\left(\pi\left(s_2 y + p_2\right)\right)\right). \end{aligned} \tag{32}$$

The following parameters were used in our simulations: $p_1 = 0.825$, $p_2 = 1.375$, $s_1 = 4p_1$ and $s_2 = 4p_2$. The post parametrised according to these values has height 1.0 and is shown in Fig. 6. Unlike the geometries considered in previous simulation studies of PABN behaviour [39, 41], where the posts were approximated either as rectangular

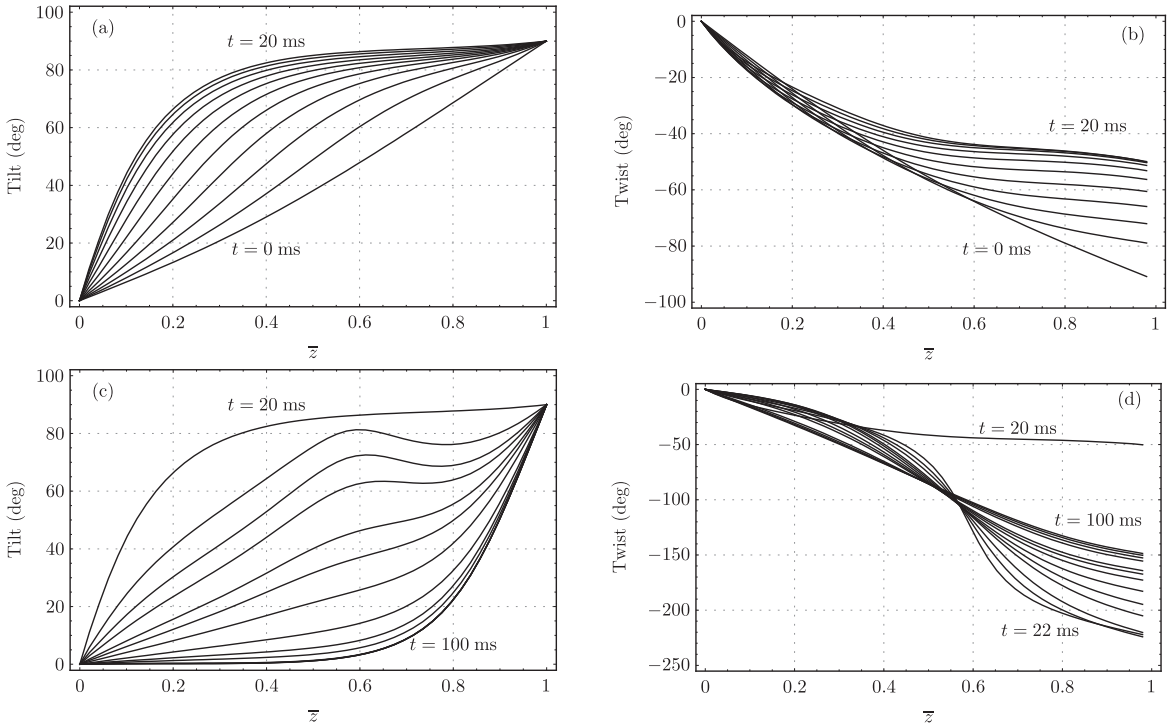

FIG. 3: Time evolution of the director twist and tilt angle profiles when the low-frequency voltage is applied (a,b) and when the high-frequency voltage is applied (c,d).

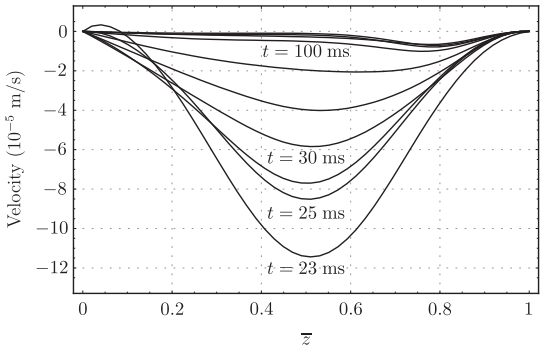

FIG. 4: Time evolution of the x-velocity across the CHAN cell as a function of reduced distance $\overline{z}$.

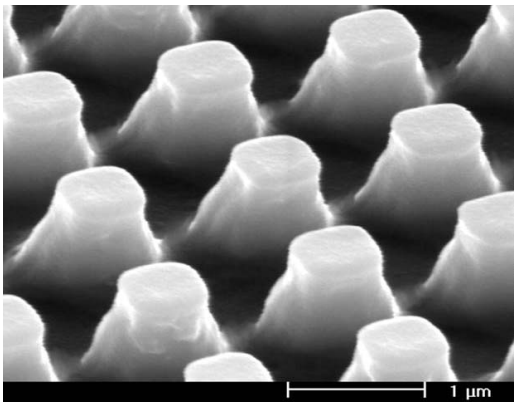

FIG. 5: The PABN device [38, 39].

bars or rectangular bars with rounded corners, this geometry is smooth and so avoids the effects of unrealistically sharp substrate features. Further, since the edges of the posts considered here are slightly asymmetric, there is not necessary to impose the direction of director tilt, as was done in the dynamic finite element simulation of Ref [42].

The post was modelled as an isotropic dielectric material with permittivity $\epsilon = 5.0$. The same dielectric constant was used for a $0.5\,\mu$m layer immediately adjacent to the post in order to represent the bottom transparent electrode of the PABN device. We have not represented the top electrode in our simulations, since doing so would introduce an unnecessary computational effort without making any practical difference, given the uniform field and director arrangements in this region.

We applied an external field across the model cell by fixing the potential on the ground electrode and on the upper homeotropic layer of the LC. The bottom electrode was set to have zero potential, the upper plate potential being set to $+20\,$V. During each time step, Maxwell's equations of electromagnetism were solved to determine the electric field inside the PABN cell. The external potential difference was applied for 3 ms and, after its removal, the LC was allowed to relax into an equilibrium configuration. The LC was taken to have negative dielectric anisotropy, which was set to $\Delta\epsilon =$

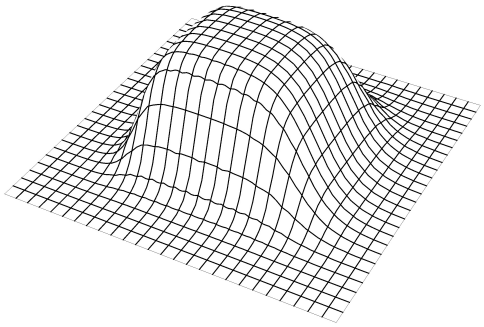

FIG. 6: An example of the analytical rectangular post shape given by eq. (32), with $p_1 = 0.825$, $p_2 = 1.375$, $s_1 = 4p_1$ and $s_2 = 4p_2$.

-4.85. The elastic constants were set to ($K_{11} = 13.7$, $K_{22} = 7.3$, $K_{33} = 22.1$, $K_{24} = 3$) $\times 10^{-12}$ N and the following set of Landau thermotropic coefficients was used: $\alpha_F = 65000\ \mathrm{J\,m^{-3}\,K^{-1}}$, $\beta_F = 533000\ \mathrm{J\,m^{-3}}$ and $\gamma_F = 975000\ \mathrm{J\,m^{-3}}$. In order to impose planar degenerate anchoring on the post surface, we used the free energy term given by eq. (7). In this, we set $c_1 = -80{\cdot}10^{-5}\ \mathrm{J/m^2}$ and $c_2 = c_3 = 0$. This value of c_1 was found to be strong enough to maintain planar alignment but not so strong that the surface nodes showed marked biaxiality.

In order to simulate the $\mathcal{T}$ – $\mathcal{P}$ transition, we took an equilibrated $\mathcal{T}$ configuration system and set the potential of the upper plate to +20 V. Fig. 7 shows a series of snapshots of the director field along the cross-section of the post's diagonal during the subsequent $\mathcal{T}$ – $\mathcal{P}$ transition. Fig. 8 shows snapshots of the LC director on the PABN post itself. The corresponding snapshots in Figs. 7 and 8 were taken at the same moments in time.

The snapshots show that, following application of the electric field, the bulk LC quickly reoriented itself into a planar arrangement due to the negative dielectric anisotropy of the simulated LC. The director field of the PABN post itself, on the other hand, showed insignificant changes on this time-scale, as can be seen in Fig. 8.2. This was due to the effects of the LC surface viscosity, which made this region respond more slowly to external influences. If the applied electric field was removed at this point, the director field was found to revert to the original tilted state $\mathcal{T}$. This is consistent with experimental observations in which the applied field pulse is too short-lived for the device switching to latch. As a technical point, we note that, despite our use of a substrate-localised description of surface viscosity, we have not observed any numerical instabilities following the application of the electric field [29]. Presumably, this is due to the relatively slow switching in this system [43].

Continued application of the applied electric field, however, caused the LC on the post's surface to reorient into the planar configuration, as can be seen in Figs. 8(3-6). This led to a consequent realignment of the adjacent bulk LC, which transformed from an inflection-like configuration in-between the posts into a $\bigcup$-like one. Fig. 8 depicts the PABN post from such an angle that the post's edge, which hosts a defect line in the planar state, is clearly visible. Initially, when the LC on the post just starts to adopt the planar configuration, the LC on the edge still maintains the 'tilted state' arrangement. Later, though, the adjacent faces become increasingly planar aligned, and the defect line develops along this edge. The finite element simulations of Ref [42] found that, for square post shapes, the mechanism of the $\mathcal{T}$ – $\mathcal{P}$ transition was dominated by point defects initially at the upper and lower corners of this edge: the switching was founded on the lower defect migrating up the post edge and annihilating with the upper defect. For the smoother post profile considered here, however, the locations and mobilities of these orientational defects are seen to be rather different. Particularly, the upper defect is initially located on the top of the post rather than at the upper corner of the trailing edge. Furthermore, it migrates significantly during the switching process, as is shown clearly in the first three images in Fig. 6. We have found that this qualitative description holds for a range of post shapes. Thus, while the post geometry affects the relative and absolute stabilities of the two states, it does not appear to affect the $\mathcal{T}$ – $\mathcal{P}$ switching mechanism.

When the electric field was completely removed, the LC in these simulations relaxed into the planar state. It should be noted that the effective optical switching between these states was much faster than the latching time. This is because the bulk LC was rapidly reoriented into the planar state by the applied electric field. The later stages of this switching, i.e. the reorientation of the LC in the post region, were crucial for zero-field stabilisation of the planar state but did not lead to significant optical change.

VII. CONCLUSIONS

In this paper, we have presented a generalisation of the MSPH technique capable of simulating static and dynamic LC behaviour. This generalised method has then been tested by comparing its outputs with previous continuum treatments of two pseudo 1-dimensional device-switching scenarios. In both cases, the MSPH simulations exhibited the expected qualitative behaviour and showed minor quantitative modifications consistent with the use of a Qian-Sheng, rather than an ELP description of nematodynamics. Alternative mesh-free and particle based approaches, such as SPH and DPD, have not proved sufficiently robust to yield a simulation model capable of fully representing such behaviour. We then have studied the switching process in the PABN device. In this, we have achieved the forward $\mathcal{T}$ – $\mathcal{P}$ switching direction, in which the system equilibrated into the $\mathcal{P}_1$ state after the external field was removed provided that the field pulse was sufficiently long-lived. The core mechanism underlying this switching was found to be a slow reorientation of the LC on the post surface.

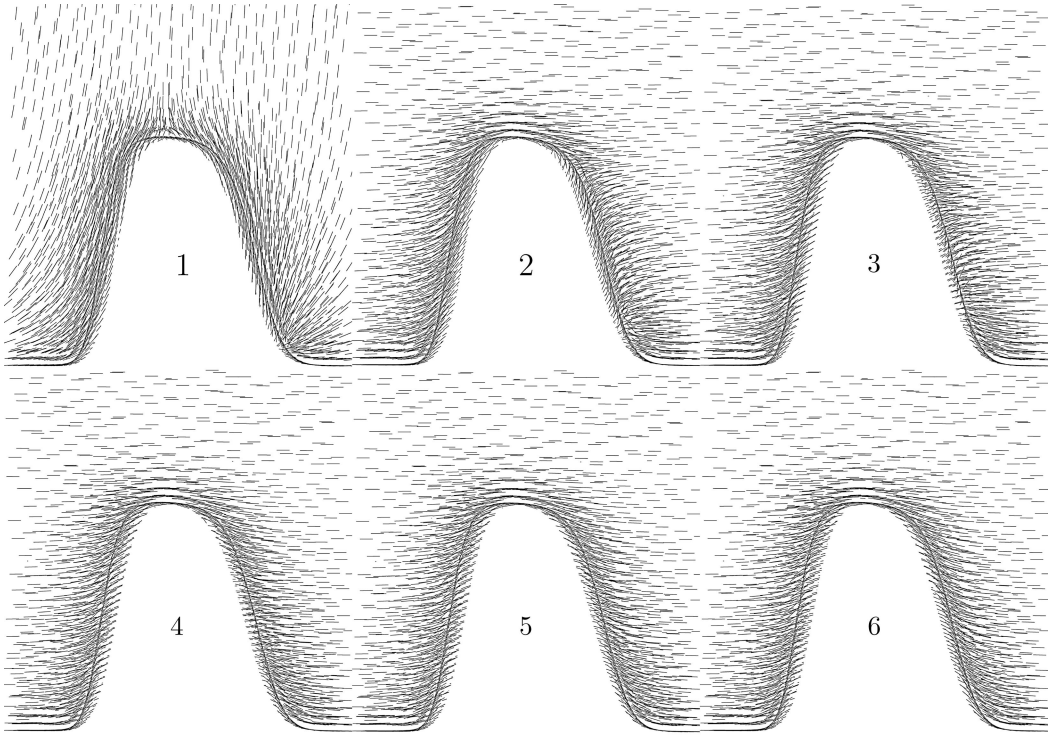

FIG. 7: Series of snapshots depicting snapshots of the director alignment in cross-sections of the post's diagonal during switching between the tilted and planar states of the PABN device. In these, $t_1 = 0\,\text{ms}$, $t_2 = 0.9\,\text{ms}$, $t_3 = 1.4\,\text{ms}$, $t_4 = 1.5\,\text{ms}$, $t_5 = 2.5\,\text{ms}$, $t_6 = 3.0\,\text{ms}$

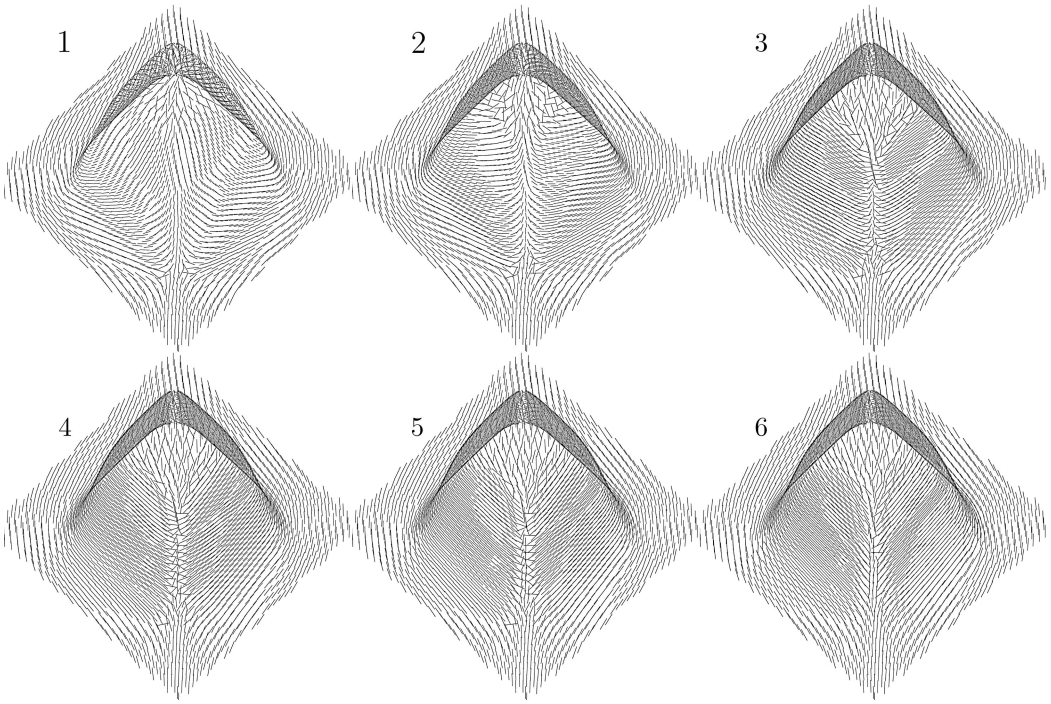

FIG. 8: Series of snapshots depicting snapshots of the director alignment in the post's surface during switching between the tilted and planar states of the PABN device. In these, $t_1 = 0\,\text{ms}$, $t_2 = 0.9\,\text{ms}$, $t_3 = 1.4\,\text{ms}$, $t_4 = 1.5\,\text{ms}$, $t_5 = 2.5\,\text{ms}$, $t_6 = 3.0\,\text{ms}$

The motivation for developing this alternative approach for nematodynamics simulation stems from a desire to open up certain problems which are inaccessible to other current approaches. Here, we have shown that the MSPH approach appears capable of manifesting a full Qian-Sheng + LdG representation whilst retaining the fundamental simplicity of implementations associated with mesh-free methods. Further, extension from 1-d to full 3-d simulations is straightforward to implement.

Importantly, the method is intrinsically multi-scale in that the sampling point density does not need to be fixed. Thus, unlike finite element and Lattice Boltzmann approaches, it is straightforward to concentrate sampling (and computational effort) in regions of interest (e.g. at surfaces, around defects). It is also possible to incorporate thermal fluctuations into MSPH methods. These properties raise the prospect of MSPH methods providing a useful basis for hybrid simulation approaches. As alluded to in previous sections, the methodology is equally applicable to alternative underlying descriptions such as microscopically derived descriptions of thermal response or additional physical features in the bulk and/or surface terms. This will aid in achieving consistency of description across any overlap regions in any possible hybrid simulation scheme. A related observation that arises when considering multi-scale modelling in a nematic liquid crystal context is that there appears to be a strong case for introducing some length-scale dependence in the order-field description.

In future work, we shall exploit the potential of this new method more fully by applying it to further nematodynamic systems in which order parameter variation and boundary complexity significantly effect system behaviour. This will include scenarios in which LC defects play a significant role in either the static or the dynamic behaviour, such as LC colloids and bistable switching devices.

VIII. ACKNOWLEDGEMENTS

MY acknowledges financial support from Sheffield Hallam University and Hewlett Packard Laboratoties. This work has benefitted from discussions with Ian Halliday, Tim Spencer and Karl Travis and arose from ideas initially raised by Kevin Good.

[1] C. M. Care and D. J. Cleaver, Reports on Progress in Physics **68**, 2665 (2005).
[2] D. Frenkel, Molecular Physics **60**, 1 (1987).
[3] R. Berardi and C. Zannoni, Journal of Chemical Physics **113**, 5971 (2000).
[4] L. A. Madsen, T. J. Dingemans, M. Nakata, and E. T. Samulski, Physical Review Letters **92**, 145505 (2004).
[5] B. R. Acharya, A. Primak, and S. Kumar, Physical Review Letters **92**, 145506 (2004).
[6] C. V. Brown, M. J. Towler, V. C. Hui, and G. P. Bryan-Brown, Liquid Crystals **27**, 233 (2000).
[7] T. J. Spencer and C. M. Care, Physical Review E **74**, 061708 (2006).
[8] I. Musevic, M. Skarabot, U. Tkalec, M. Ravnik, and S. Zumer, Science **313**, 954 (2006).
[9] L. B. Lucy, Astronomical Journal **82**, 1013 (1977).
[10] R. A. Gingold and J. J. Monaghan, Monthly Notices of the Royal Astronomical Society **181**, 375 (1977).
[11] J. J. Monaghan, Journal of Computational Physics **110**, 399 (1994).
[12] J. W. Swegle and S. W. Attaway, Computational Mechanics **17**, 151 (1995).
[13] J. K. Chen, J. E. Beraun, and T. C. Carney, International Journal for Numerical Methods in Engineering **46**, 231 (1999).
[14] P. W. Randles and L. D. Libersky, Computer Methods in Applied Mechanics and Engineering **139**, 375 (1996).
[15] G. R. Liu and M. B. Liu, *Smoothed Particle Hydrodynamics: A Meshfree Particle Method* (World Scientific, 2003).
[16] W. K. Liu, S. Jun, and Y. F. Zhang, International Journal for Numerical Methods in Fluids **20**, 1081 (1995).
[17] G. M. Zhang and R. C. Batra, Computational Mechanics **34**, 137 (2004).
[18] M. B. Liu and G. R. Liu, Applied Numerical Mathematics **56**, 19 (2006).
[19] M. B. Liu, W. P. Xie, and G. R. Liu, Applied Mathematical Modelling **29**, 1252 (2005).
[20] R. C. Batra and G. M. Zhang, Computational Mechanics **40**, 531 (2007).
[21] G. M. Zhang and R. C. Batra, Journal of Computational Physics **222**, 374 (2007).
[22] R. C. Batra and G. M. Zhang, Journal of Computational Physics **201**, 172 (2004).
[23] T. Z. Qian and P. Sheng, Physical Review E **58**, 7475 (1998).
[24] P. G. D. Gennes and J. Prost, *The Physics of Liquid Crystals* (Clarendon press, Oxford, 1993), 2nd ed.
[25] E. F. Gramsbergen, L. Longa, and W. H. Dejeu, Physics Reports **135**, 195 (1986).
[26] T. J. Sluckin and A. Poniewierski, *Chap. 5* (Wiley, Chichester, 1986), pp. 215–253, Fluid Interfacial Phenomena.
[27] C. M. Care, I. Halliday, and K. Good, Journal of Physics-Condensed Matter **12**, L665 (2000).
[28] M. Vilfan, I. D. Olenik, A. Mertelj, and M. Copic, Physical Review E **63**, 061709 (2001).
[29] A. M. Sonnet, E. G. Virga, and G. E. Durand, Physical Review E **62**, 3694 (2000).
[30] A. Fang, T. Qian, and P. Sheng, Physical Review E **78**, 061703 (2008).
[31] J. P. Morris, P. J. Fox, and Y. Zhu, Journal of Computational Physics **136**, 214 (1997).
[32] J. J. Monaghan and J. C. Lattanzio, Astronomy and Astrophysics **149**, 135 (1985).
[33] I. W. Stewart, *The Static and Dynamic Continuum The-*

ory of Liquid Crystals: A Mathematical Introduction (Taylor & Francis Ltd, 2003).
[34] H. J. Deuling, Molecular Crystals and Liquid Crystals **19**, 123 (1972).
[35] H. J. Coles, Molecular Crystals & Liquid Crystals **49**, 67 (1978).
[36] S. A. Jewell and J. R. Sambles, Physical Review E **73**, 011706 (2006).
[37] S. A. Jewell and J. R. Sambles, Molecular Crystals and Liquid Crystals **477**, 551 (2007).
[38] S. Kitson and A. Geisow, Applied Physics Letters **80**, 3635 (2002).
[39] A. Majumdar, C. J. P. Newton, J. M. Robbins, and M. Zyskin, Physical Review E **75**, 051703 (2007).
[40] M. V. Yakutovich, C. J. P. Newton, and D. J. Cleaver, Molecular Crystals and Liquid Crystals **502**, 245 (2009).
[41] S. C. Kitson and A. D. Geisow, Molecular Crystals and Liquid Crystals **412**, 153 (2004).
[42] E. Willman, F. A. Fernandez, R. James, and S. E. Day, Journal of Display Technology **4**, 276 (2008).
[43] G. Barbero and L. Pandolfi, Physical Review E **79**, 051701 (2009).